PHYSICAL REVIEW A **69**, 062715 (2004)

Electron capture and excitation in collisions of $O^+(^4S, ^2D, ^2P)$ with H_2 molecules

Lukáš Pichl*
Foundation of Computer Science Laboratory, University of Aizu, Tsuruga, Ikki, Aizuwakamatsu, Fukushima 965-8580, Japan

Yan Li, Heinz-Peter Liebermann, and Robert J. Buenker
Theoretische Chemie, Bergische Universitaet, Gesamthochschule Wuppertal, Fachbereich 9, Gaussstrasse 20, D-42119 Wuppertal, Germany

Mineo Kimura
Graduate School of Sciences, Kyushu University, Hakozaki, Fukuoka 812-8581, Japan

(Received 9 January 2003; revised manuscript received 2 June 2003; published 17 June 2004)

Using an electronic-state close-coupling method, we treated the electron capture and excitation processes of O^+ ions both in ground state $O^+(^4S)$ and metastable states $O^{+*}(^2D)$ and $O^{+*}(^2P)$ in collisions with the H_2 molecule. In the ground-state projectile energy region considered (from 50 eV/amu to 10 keV/amu), the experimental data vary by orders of magnitude: our results smoothly connect to the data by Flesch and Ng [J. Chem. Phys. **94**, 2372 (1991)] and Xu *et al.* [J. Phys. B **23**, 1235 (1990)] at low energy and agree with Phaneuf *et al.* [Phys. Rev. A **17**, 534 (1978)] in the high-energy region. The present values differ from Sieglaff *et al.* [Phys. Rev. A **59**, 3538 (1999)] and Nutt *et al.* [J. Phys. B **12**, L157 (1979)], especially in the energy region below 1 keV/amu. We provide the first calculated state-resolved cross sections of electron capture and target-projectile electronic excitations for the $O^+(^4S, ^2D, ^2P)$-H_2 collision system.

DOI: 10.1103/PhysRevA.69.062715 PACS number(s): 34.50.Gb, 34.70.+e, 52.27.−h, 98.38.Bn

I. INTRODUCTION

A survey of the literature on the measured $O^+(^4S)$-H_2 total charge transfer cross sections, as published since the 1970s until 2002, raises an interesting question on the origin of the orders of magnitude discrepancy which still persists in the experimental data [1–13]. The collision of $O^+(^4S)$ ground-state ions with H_2 has been measured many times. This is not only because the resulting charge-transfer process is known to be important in astronomy [14–16], fusion science [17], and chemistry [18], but especially since resolving the above discrepancy remains a challenge in both experiment and theory.

Several experimental techniques were employed to measure the $O^+(^4S)$-H_2 total charge-transfer cross section as classified by the $O^+(^4S)$ production mechanism. First, dissociative ionization of CO molecules by electron impact with collision energy below the metastable production threshold was used by Moran and Wilcox [4], Kusakabe *et al.* [6–8], and Hoffman *et al.* [9]. Sieglaff *et al.* [5] filtered out the metastable $O^{+*}(^2D)$ and $O^{+*}(^2P)$ ions from a mixture containing the $O^+(^4S)$ ions by using charge-transfer collisions with N_2. Flesh and Ng [2] and Irvine and Latimer [3] produced ground-state $O^+(^4S)$ ions by the dissociative photoionization of O_2. Finally, Xu *et al.* [1] and Nutt *et al.* [11] used beam attenuation curves to distinguish the $O^+(^4S)$ data.

In the charge-transfer cross-section measurements of metastable $O^{+*}(^2D, ^2P)$ ions, Xu *et al.* [1] relied on the attenuation curve method and Sieglaff *et al.* [5] used a mixed-state ion beam with a defined $O^+(^4S)$ abundance ratio, while Li *et al.* [10] employed the dissociative charge transfer in collisions of Ne^+ and He^+ with O_2. By using rf octopole ion trap techniques, Li *et al.* obtained state-specific $O^{+*}(^2D)$ and $O^{+*}(^2P)$ ion beams.

In the case of the $O^+(^4S)$ ion, there are two charge-transfer cross-section data sets, which differ by an order of magnitude. The first set is characterized by low cross-section values, such as in the experiments of Flesh and Ng [2]. Measurements by Xu *et al.* [1], Irvine and Latimer (below 25 eV/amu) [3], and Moran and Wilcox [4] fall in this data set. The second set of measurements is characterized by substantially larger cross sections for collision energy above 10 eV/amu, as represented in the data by Nutt *et al.* [11]. Higher cross-section magnitudes, in the range from 10^{-16} to 10^{-15} cm^2, were found in recent measurements by Sieglaff *et al.* [5], Kusakabe *et al.* [6–8], and older data by Hoffman *et al.* [9]. An important feature in these data is a pronounced dip in the total charge-transfer cross section at the projectile energy ~100 eV/amu.

In the case of the $O^{+*}(^2P)$ and $O^{+*}(^2D)$ ions, the experimental results vary to much less extent. The total charge-transfer cross sections flatten at about 10^{-15} cm^2 approximately from 10^{-1} to 10^4 eV/amu, with discrepancies of a factor of 2. Li *et al.* measured low-energy charge-transfer cross sections separately for the $O^{+*}(^2P)$ and $O^{+*}(^2D)$ ions below 6 eV/amu, while the other data at higher energies correspond to an $O^{+*}(^2D, ^2P)$ mixture.

From a theorist's point of view, this system is challenging since there has been no rigorous calculation of the O^+-H_2 collision process available. An accurate *ab initio* treatment is necessary to treat the collision intermediate $(H_2O)^+$ water molecular ion, which governs the details of electron capture

---

*Corresponding author. FAX: +81-242-37-2734. Electronic address: lukas@u-aizu.ac.jp

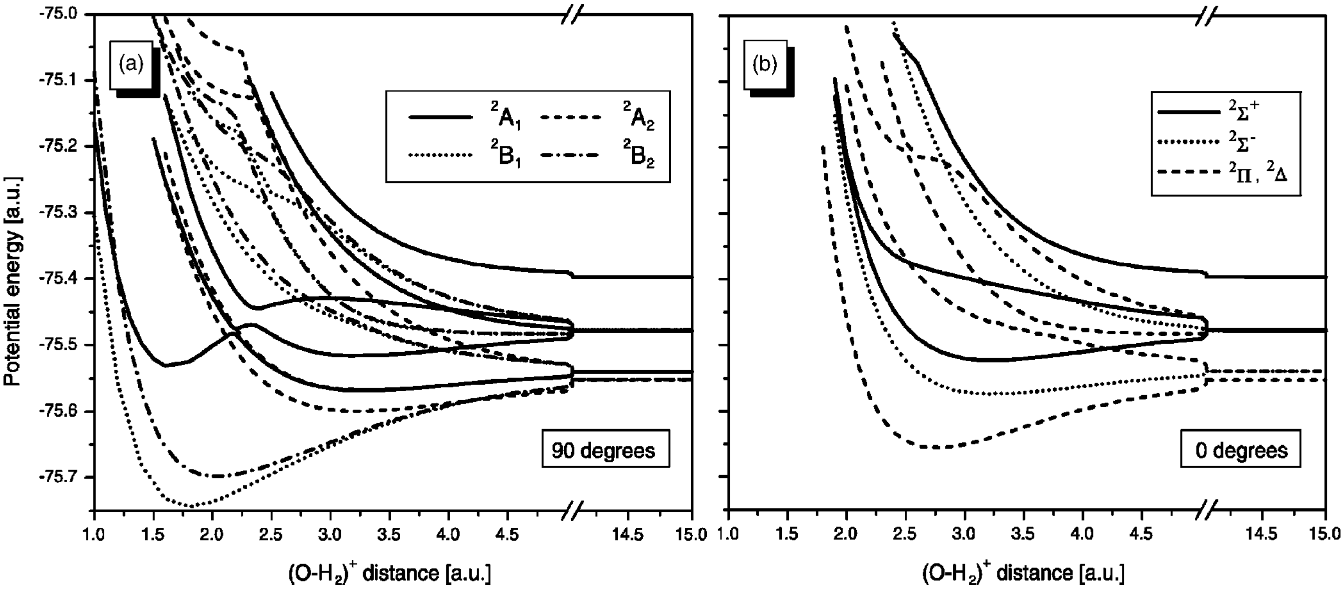

FIG. 1. $(H_2O)^+$ adiabatic potential curves: (a) $\gamma = \pi/2$ ($^2A_1$, $^2A_2$, $^2B_1$, $^2B_2$), (b) $\gamma = 0$ ($^2\Sigma^+$, $^2\Sigma^-$, $^2\Pi$, $^2\Delta$). The assignment of asymptotic states to O^+ and O is indicated in Table II. Vertical scale labels are the same for (a) and (b).

and excitation processes. Further, the theory of ion-molecule collision processes is important for its applications in ion source production, plasma physics, the chemistry of interstellar clouds, and astronomy [20]. For instance, water vapor is abundant in comets, and its absorption of ultraviolet radiation yields excited quasimolecular H_2O^+ ions in cometary tails (other frequent constituents are also carbon monoxide and cyanogen ions). These emit light, dissociate, and interact with other ions from the solar wind [20].

In fusion, undesirable H_2O^+ ions are often created during primary plasma heating by neutral atoms [21]. Their formation occurs as follows. First, the ion source produces not only the protons, but also H_2^+ and H_3^+ ions, which are all accelerated. Then, due to possible leaks in water-cooled acceleration grids or in systems with oxygen impurities in gaseous neutralizers, H_2O^+ ions are formed. Their final dissociation in the neutralizer yields hydrogen atoms at fractions of the extraction energy, which decreases the efficiency of plasma heating. In order to describe these complex phenomena in detail, cross sections of all relevant processes need to be determined.

In this paper, we have theoretically studied the dynamics of electron capture and target-projectile excitation and deexcitation processes in collisions of $O^{+*}(^2P)$ and $O^{+*}(^2D)$ with H_2. The effects of metastable impurities on the experimental $O^+(^4S)$ charge-transfer cross section are also addressed. We explore the distribution of final electron-capture states based on the collision parameters. In Sec. II, the theoretical method is reviewed: first the *ab initio* calculations of molecular states by the multireference single- and double-excitation space configuration interaction (MRD-CI) method, then the collision dynamics by the electronic-state close-coupling (ESCC) method. In the ESCC method, the electronic states of the collision intermediate, the H_2O^+ molecular ion, are used as an expansion basis for the electronic wave functions augmented with the atomic-type electron translation factor (ETF) in order to impose the correct scattering boundary conditions.

The H_2O^+ potential energy curves and coupling elements in doublet and quartet states are computed with high accuracy for more than 1500 collision geometries, then a 10 000–point two-dimensional (2D) grid is used to obtain the cross sections. This represents in total an extensive computation of more than 2 months in CPU time. Section III contains our results; we discuss the capture state-resolved charge transfer by $O^+(^4S)$, $O^{+*}(^2P)$, and $O^{+*}(^2D)$ ions, electronic excitations, and the discrepancies seen in the $O^+(^4S)$ experiments. The final remarks in Sec. IV conclude the paper. Atomic units are used throughout.

II. THEORETICAL FRAMEWORK

In this section, (1) *ab initio* quantum chemical treatment of the three-center molecular ion and (2) electronic-state close-coupling methods are reviewed.

A. Electronic states of the H_2O^+ molecule

The potential surfaces for the H_2-O^+ system (cf. Fig. 1 and Ref. [22]) were obtained for a variety of electronic states in $^2A_1$, $^2A_2$, $^2B_1$, $^2B_2$, $^4A_2$, and $^4B_1$ molecular symmetries by *ab initio* configuration interaction (CI) calculations in multireference single- and double-excitation spaces, by using the MRD-CI series of programs [23–26]. For the hydrogen atoms, a Gaussian $(6s3p2d1f)$ basis contracted to $[4s3p2d1f]$ is used, while a $(12s6p3d2f)$ basis contracted to $[5s4p3d2f]$ was employed for the oxygen atom. Dunning's basis sets for H and O atoms are of the cc-pVQZ type [27]. The OH_+^2 molecular Rydberg states are described by using additional diffuse $(2s2p2d)$ sets of functions centered on the oxygen atom [28]. The number of configurations in the multireference single- and double-excitation space varies with the

TABLE I. $(OH_2)^+$ molecular states coupled to the ground state $O^+({}^4S)$.

State	${}^3P({}^4B_1)$	${}^3P({}^4A_2)$	${}^4S({}^4B_1)$	${}^5S({}^4A_2)$	${}^3S({}^4A_2)$
$R\to\infty$	O/H_2^+	O/H_2^+	$O^+/H_2^*(3\Pi)$	O/H_2^+	O/H_2^+

symmetry of the electronic states, not exceeding 500 000 for the selection threshold 2.0×10^{-7} a.u. used in the present calculation. The effect of all unselected configurations is checked by using the perturbative energy extrapolation procedure [26]. The resulting highly correlated wave functions are used to obtain nonadiabatic coupling matrix elements [29]. The origin of electronic coordinates is placed at the molecular center of mass for all geometries. We have used atomic-type electron translation factor corrections [30], which are equivalent to the dipole coupling in the asymptotic region. This type of ETF cannot be optimal since it ignores the molecular effect of the H_2 molecule. Nevertheless, it recovers the correct asymptotic behavior by removing the spurious constant terms, and hence it should provide a reasonable base for dynamical argument.

The potential surfaces are computed as a function of the distance $\vec{R}$ between the O nucleus and the center of mass of the H_2 target molecule, while holding the latter's bond length $|\vec{r}|$ fixed at its equilibrium value. The internuclear separation is $r=1.4$ a.u., at which the electronic ground-state energy reaches its minimum value and the vibrational wave function has a peak. Similar potential surfaces were obtained for $r=1.6$ a.u. in order to estimate the effects of target vibrations and out-of-the-equilibrium geometries. This is discussed more in detail in Sec. III F. The surfaces are projected on the planes $\gamma=\angle(\vec{R},\vec{r})=\text{const}$, for $\gamma=0$, $\pi/4$, $\pi/2$. The results for the doublet states $(r=1.4\text{ a.u.},\gamma=0,\pi/2)$ are shown in Fig. 1.

Let us note that the phase factors of electronic eigenfunctions ϕ_i are arbitrary in each point of space, which often results in random signs of the coupling terms C_{ij}. When computing the full coupling matrix, we consistently track and fix the incorrect coupling signs $\pm C_{ij}$ either by replacing $\phi_i\to-\phi_i$ or $\phi_j\to-\phi_j$. This procedure is unique as long as $|C_{ij}|$ does not vanish. Zero values of $|C_{ij}|$ appear near sharp avoided crossings, where we decide the correct coupling sign by fitting to Fano profiles. If there still remains an ambiguity, $\pm C_{ij}$ is determined by the sign of electronic overlaps $\langle\phi_i(R)|\phi_i(R+\Delta)\rangle$ and $\langle\phi_j(R)|\phi_j(R+\Delta)\rangle$. Finally, the sign of small coupling values in the asymptotic region typically does not oscillate and the magnitude monotonically decreases. Further details concerning the present theoretical method, including calculation of nonadiabatic coupling matrix elements [24,26], can be found in earlier work [29].

The nonadiabatic couplings between the $O^+({}^4S)$ ground state and the other states in Table I are published in Ref. [22]. In Fig. 1, the metastable and charge transfer potential curves are plotted for (a) the ${}^2A_1$, ${}^2A_2$, ${}^2B_1$, and ${}^2B_2$ symmetries with $\gamma=\pi/2$ and for (b) the ${}^2\Sigma^-$, ${}^2\Sigma^+$, ${}^2\Pi$, and ${}^2\Delta$ molecular symmetry manifolds with $\gamma=0$. These states are summarized in Table II and their representative couplings are shown in Fig. 2. Figure 3 shows analogous diabatic potential curves and diabatic couplings (doublet A_2 symmetry with $\gamma=\pi/2$). It is clearly demonstrated in Figs. 2 and 3 that the diabatic couplings are very smooth as compared to the sharp derivative terms in adiabatic basis.

TABLE II. Assignment of $(OH_2)^+$ molecular states corresponding to $O^{+*}({}^2D)$ and $O^{+*}({}^2P)$ and their charge-transfer states (ordered by increasing asymptotic energy from left to right; cf. Fig. 1).

$\gamma=\pi/2$[a]					
${}^2A_1$	$O^+({}^2D)$	$O({}^1D)$	$O({}^1D)$	$O^+({}^2P)$	$O({}^1S)$
${}^2A_2$	$O({}^3P)$	$O^+({}^2D)$	$O^+({}^2D)$	$O({}^1D)$	
${}^2B_1$	$O({}^3P)$	$O^+({}^2D)$	$O({}^1D)$	$O^+({}^2P)$	
${}^2B_2$	$O({}^3P)$	$O^+({}^2D)$	$O({}^1D)$	$O^+({}^2P)$	
$\gamma=0$					
${}^2\Sigma^+$	$O({}^1D)$	$O^+({}^2P)$	$O(1S)$		
${}^2\Sigma^-$	$O({}^3P)$	$O^+({}^2D)$			
${}^2\Delta$	$O^+({}^2D)$	$O({}^1D)$			
${}^2\Pi$	$O({}^3P)$	$O^+({}^2D)$	$O({}^1D)$	$O^+({}^2P)$	

[a] O^+ is assigned to the H_2 ground state; O is assigned to various $H_2{}^{+*}$ nonequilibrium states.

For $\gamma=0$, the mixing molecular states are (1) three Σ^+ states $O({}^1S)$, $O({}^1D)$, and $O^{+*}({}^2P)$, (2) two Σ^- states $O({}^3P)$ and $O^{+*}({}^2D)$, (3) four Π states $O({}^3P)$, $O({}^1D)$, $O^{+*}({}^2D)$, and $O^{+*}({}^2P)$, and (4) two Δ states $O({}^1D)$ and $O^{+*}({}^2D)$. Finally, we computed the $\gamma=\pi/4$ potential energy surfaces for the lowest C_s symmetry and discuss the effects of the collision angles in Sec. III G.

In the following, the adiabatic electronic basis is transformed and the close-coupling method is applied.

B. Collision dynamics by the close-coupling method

The scattering dynamics for ion-diatomic collisions was formulated quantum mechanically in the review article by Sidis, based on the electronic state expansion of the total wave function and applied extensively since then [31]. Using sudden approximation for target vibrations and rotations and the eikonal approach, the stationary Schrödinger equation can be reduced to sets of first-order differential equations for electronic-state amplitudes at fixed geometries as explained below. Only collisions in the energy region above 50 eV/amu are considered here.

Following Ref. [31], we assume that the collision time is much shorter than the characteristic rotation time of the target molecule, which is already satisfied for energy above 0.1 eV/amu, and thus the rotational state of the *target* molecule may not change during the collision. The method described by Sidis [31] further requires the centrifugal-sudden condition—i.e., the relative radial motion of the ion and molecule to be much faster than their angular relative motion. Although this allows for additional simplifications in the coupled equations, it cannot be satisfied in the present energy region. Moreover, since such condition implies a *complete* neglect of rotational couplings, the formalism in Ref. [31] does not recover the ion-atom case [14] in the limit $r=0$

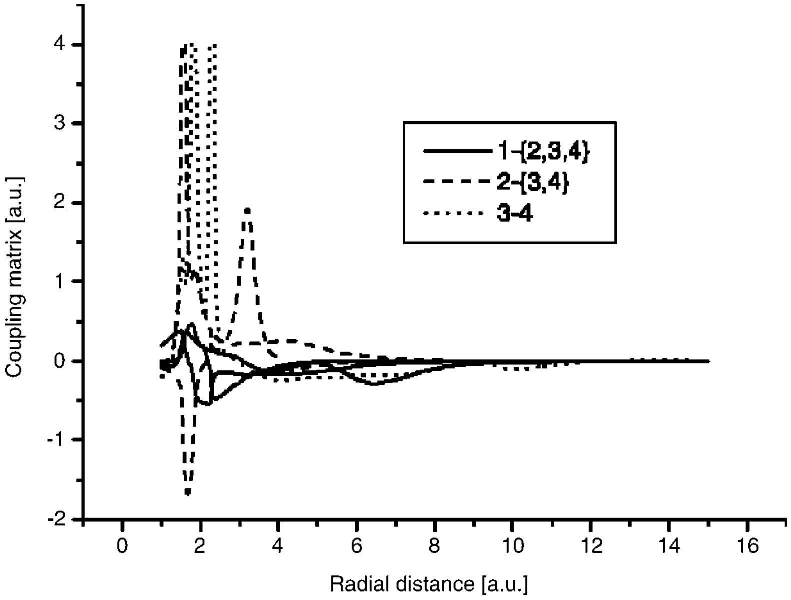

FIG. 2. $(H_2O)^+$ $(^2B_2)$ representative couplings (for $\gamma=\pi/2$). Label numbers increase with increasing asymptotic energy of the electronic state, correspondingly to Fig. 1 and Table II.

because all angular coupling components are missed. This drawback is overcome by extending the approach below.

Coriolis couplings for the ion-molecular system include rotation of the target molecule, rotation along the R axis, and their mixing terms. As the collision energy is very high relative to 0.1 eV, both the rotation of the target molecule and the mixed terms of Coriolis couplings can be neglected. In this way, we also recover the ion-atom formalism in the very limit $r=0$, when the angular and radial components of the coupling completely separate and become independent of the parameter γ in all representations.

In particular, here we adopt the fixed γ approximation, same as in the article by Sidis [31], which is based on (1) the diabatic representation, in which $\partial/\partial\gamma$ vanishes, and (2) the angular momentum decoupling scheme (discussed in detail in Ref. [32] and references therein). Unlike from Ref. [31], the relative angular motion of the impact ion and the target molecule is not ignored. The parameter γ represents a continuous averaging index corresponding to the *asymptotic* collision orientation. In the present case, the major orientation $\gamma=\pi/2$ is γ diabatic because the target is homonuclear, the case $\gamma=0$ has a zero weight, and the γ dependence of potentials and couplings in all representations is generally weaker for γ compared to R as shown in Sec. III.

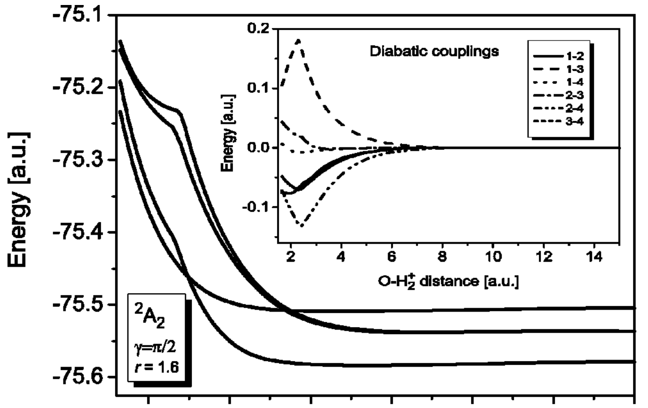

FIG. 3. Representative diabatic potentials (for $\gamma=\pi/2$) and their couplings (the inset). Label numbers increase with increasing asymptotic energy of the electronic state.

Channels included in the present calculation are OH_+^2 ($\gamma=\pi/2$: $^4A_2$, $^4B_1$, $^2A_1$, $^2A_2$, $^2B_1$, $^2B_2$; $\gamma=\pi/4$: A', A''; $\gamma=0$: $\Sigma^+,\Sigma^-,\Pi,\Delta$). All nonvanishing radial and angular couplings are included, with the exception of terms proportional to rotation along the x-component. As noted above and shown in previous studies [22,31,32], the role of target rotations is negligible. Restricting ourselves to energies about $E > 50$ eV/amu, the target vibrational motion is slow enough, and H_2 internuclear separation can be fixed at its equilibrium value. Rovibrational spacing is negligible in this energy range, and transitions are driven especially by the nonadiabatic couplings among the electronic states. In order to assess the vibrational time scales, the classical period of H_2 nuclear motion is evaluated to $T_0 \sim 320$ a.u. for $v=0$, while the projectile passes through the region of strong coupling (length ~ 0.3 a.u.) within $T_c=7$ a.u. at the lowest collision energy $E \simeq 50$ eV/amu, or faster for higher energy. Also the H_2 vibrational spacing at the lowest-energy levels is about $\Delta E_v \simeq 0.02$ a.u., corresponding to a quantum time scale $T_Q \simeq 1/\Delta E_v = 50$ a.u.—i.e., sufficiently higher than the collision times.

The coupled equations for nuclear wave functions $F_n(R)$ are solved in the diabatic basis, $F_n^{(d)}(R)=\Sigma_{n'} U_{nn'}(R) F_{n'}^{(a)}$, where $U(R)$ is a unitary matrix of the adiabatic-to-diabatic transform. In the diabatic representation, the electronic matrix elements of $\partial/\partial R$ vanish; the adiabatic potential matrix $V^{(a)}(R)$ transforms as $V^{(d)}(R)=U(R)V^{(a)}(R)U^{-1}(R)$. Using the eikonal approach, we define a collision coordinate $z=\pm(R^2-b^2)^{1/2}$ with $b=(l+1/2)/k$ to solve the further-reduced system of first-order differential equations [22]:

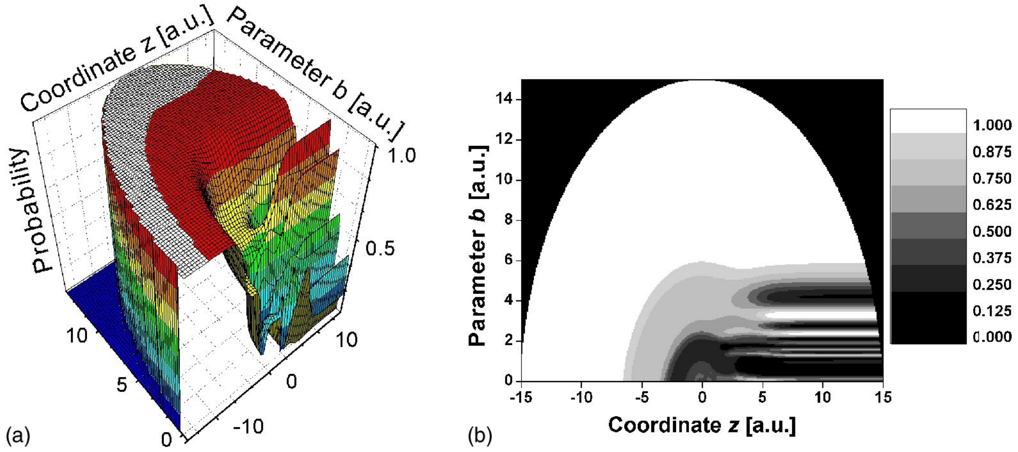

FIG. 4. SC-ESCC method: initial channel probability in ${}^2B_1$ 90° case. Collision energy is 2 keV; projectile initial state corresponds to $O^{+*}({}^2D)$. The local probability is shown vs the parameters $b \leqslant R_0$ and coordinates $z \in \langle -(R_0^2-b^2)^{1/2}, (R_0^2-b^2)^{1/2} \rangle$. (a) 3D surface. (b) Contour plot: white color corresponds to the initial $O^{+*}({}^2D)$ channel; grey to black color indicates increasing charge transfer probability. The converged values are located on the parabolic curve in the right half of this figure. Stueckelberg oscillations can be seen along this border, as b changes.

$$\left[i\frac{d}{dz}-\frac{V_{nn}(R)}{v}\right]f_n^b(z;\gamma)=\sum_{n'}{}' v_{nn'}f_n^b(z;\gamma). \qquad (1)$$

Here $v \equiv k/\mu$, $R=R(z,b)$, and $v_{nn'}(R)$ denotes both the state-to-state coupling components. Equation (1) should be solved for $z \in \langle -\infty, \infty \rangle$ with $f_{n'}^b(-\infty)=\delta_{nn'}$. The cross section for $n \rightarrow n'$ processes is obtained with formal integration over b,

$$\sigma_{nn'}(E;\gamma)=2\pi\int_0^\infty b|\delta_{nn'}-S_{nn'}^b(E;\gamma)|^2 db,$$

and averaging over γ with the weight sin γ. This summarizes the semiclassical treatment (SC-ESCC). Let us note at this point that an analogous formulation of the semiclassical approach has been developed by Errea *et al.* [33]. We solve Eq. (1) numerically in the interval $\langle -z_0, z_0 \rangle$ with $z_0=(R_0^2-b^2)^{1/2}$ and $R_0=15$. All couplings vanish for $R > R_0$. An equidistant spatial step of 3×10^{-3} a.u. is applied to z at the coupling peak regions and also to $b \in (0,15)$. Converged amplitudes $f_n^b(z_0;\gamma)$ for the initial condition $f_n^b(-z_0;\gamma)=\delta_{nn'}$ yield $S_{nn'}^b$. State-resolved cross sections are obtained by using Eq. (2). A quantal algorithm can be found in Ref. [34].

The SC-ESCC method is illustrated in Fig. 4(a). Solutions of Eq. (1) for the nuclear wave function in the initial channel $p(z,b)=|F_n^b(z;\gamma=\pi/2)|^2$ are plotted as a function of z and b for a fixed collision energy. The parabolic border of the surface corresponds to the end points $\pm z_0$, $z_0=(R_0^2-b^2)^{1/2}$; each line $b=$const is a single solution of Eq. (1), initially equal to 1 at $-z_0$. The probability is distributed to other channels as z changes through a sequence of avoided crossings, before reaching a converged value at z_0 on the right. This effect is not linear and $p(z;b)$ is not a monotonous function of z. Multiplying the converged probability $p(z_0,b)$ with b and integrating over b yields the cross section for the fixed energy. As b changes, the phase accumulated between the avoided crossings changes and produces the oscillations of $p(z_0,b)$ with b, which is clearly seen in Fig. 4(b).

III. SCATTERING DYNAMICS AND CROSS SECTIONS

In this section, state-resolved cross sections for $O^+({}^4S)$ electron capture obtained with the SC-ESCC method are calculated for the energy range $(50-10^4)$eV/amu (Fig. 5). Next, the state-resolved cross sections obtained here for processes involving $O^{+*}({}^2D)$ and $O^{+*}({}^2P)$ ions and for an efficient electronic excitation of the H_2 molecule by $O^+({}^4S)$ ion are given in Fig. 6. The effect of target ground-state vibrational motion is assessed in Fig. 7 at $r=1.6$ a.u., where the probability density reaches half of its maximum value. Figure 8 compares the angle-fixed cross sections for $\gamma=\pi/4$ and $\gamma=\pi/2$. Total charge-transfer cross-section results are compared to the available experimental data in Fig. 9 for the $O^+({}^4S)$ ion

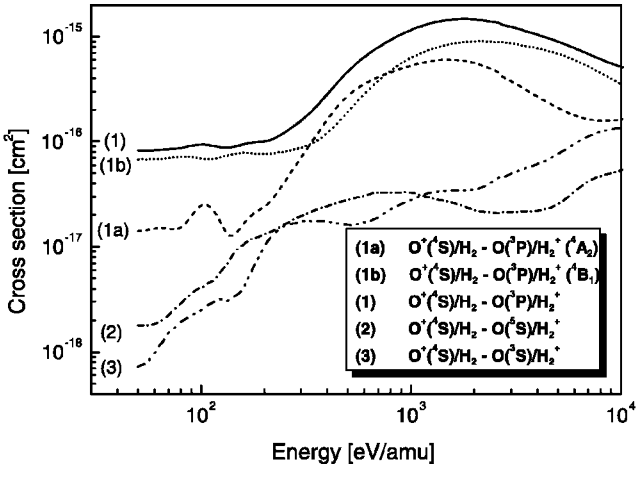

FIG. 5. State-resolved cross sections of the $O^+({}^4S)$ ground state ion ($\gamma=\pi/2$) for charge transfer to $O({}^3P)$ (1), $O({}^5S)$ (2), and $O({}^3S)$ (3).

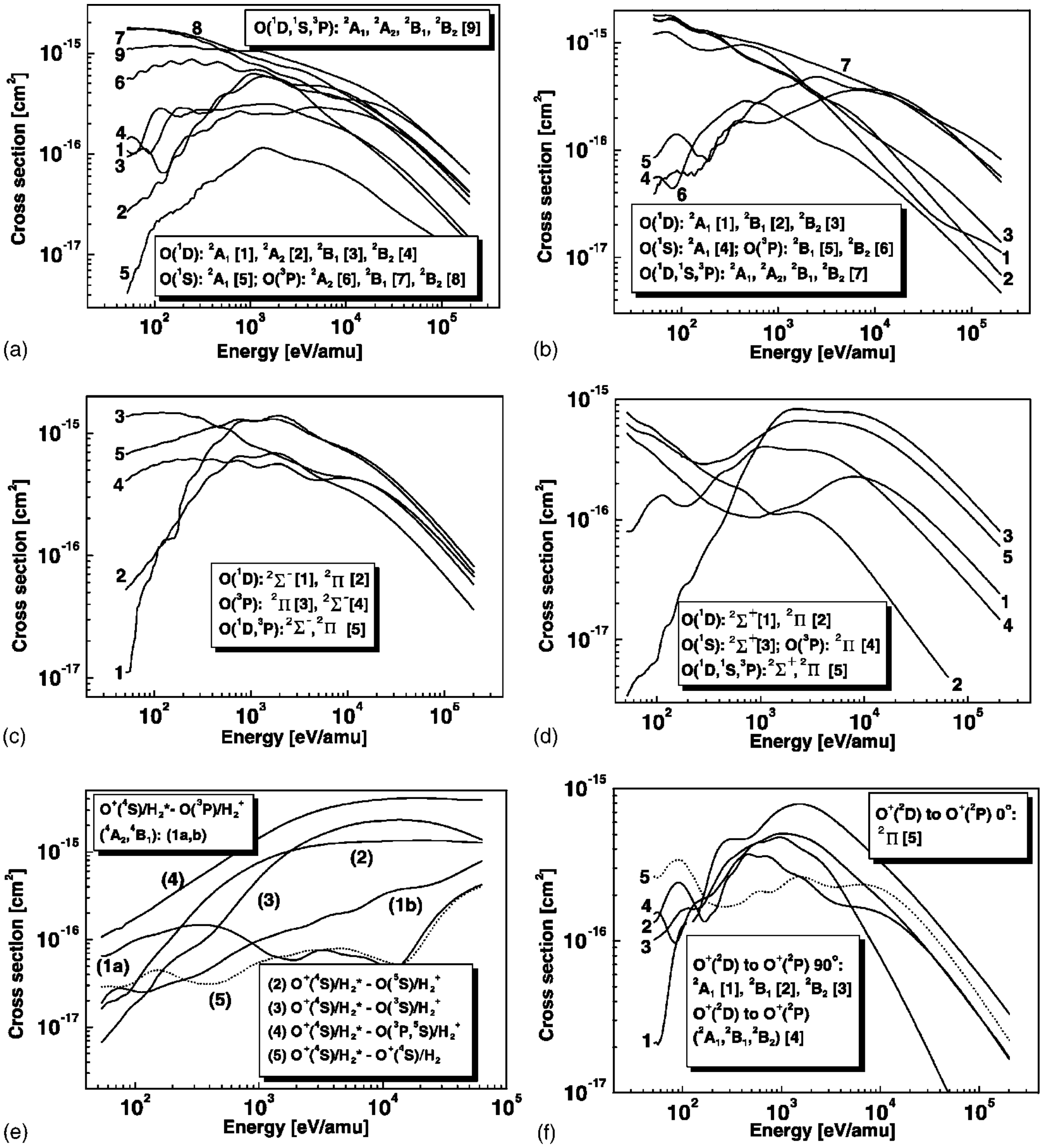

FIG. 6. State-resolved cross sections for processes involving $O^+(^2D, ^2P, ^4S)$ ions: (a) Charge-transfer cross sections for $O^{+*}(^2D)$ at $\gamma = \pi/2$. Curve 9 corresponds to the total $O^{+*}(^2D)$ charge transfer. (b) Charge-transfer cross sections for $O^{+*}(^2P)$ at $\gamma = \pi/2$. Curve 7 corresponds to the total $O^{+*}(^2P)$ charge transfer. (c) Charge-transfer cross section $\sigma(\gamma)$ for $O^{+*}(^2D)$ at $\gamma = 0$. Curve 5 is the total for $O(^1D, ^3P)$. (d) Charge-transfer cross section $\sigma(\gamma)$ for $O^{+*}(^2P)$ at $\gamma = 0$. Curve 5 is the total for $O(^1D, ^1S, ^3P)$. (e) $O^+(^4S)$ charge transfer on electronically excited $H_2^*(^3\Pi)$ (curves 1–4) and H_2 excitation by $O^+(^4S)$ impact (curve 5). (f) $O^{+*}(^2D)/O^{+*}(^2P)$ transitions at $\gamma = \pi/2$ (curves 1–4) and $\gamma = 0$ (curve 5).

and in Fig. 10 for the metastable $O^{+*}(^2D)$ and $O^{+*}(^2P)$ ions, respectively. The orientation effects are briefly discussed.

A. Electron capture by $O^+(^4S)$

The calculated electron capture cross sections for ground-state O^+ from ground-state H_2 are shown in Fig. 5. The dominant process is the capture to the $O(^3P)$ final state in $^4A_2$ and $^4B_1$ symmetries, the cross section of which flattens in the energy range (50–300) eV/amu, before growing to the maximum at around 2 keV/amu. Nonadiabatic couplings for the $O(^3P)$ final state are found to be the strongest: localized around small $R \sim 0.7$ a.u. for the quartet $^4A_2$ and relatively broad for the case of $^4B_1$. The other significant charge-transfer channels $O(^3S)$ and $O(^5S)$ are weakly coupled, and the corresponding cross sections are one to two orders of magnitude lower in the whole energy range considered. All cross sections in Fig. 5 are calculated for the perpendicular orientation $\gamma = \pi/2$. The difference of the $O(^3P)$ amplitude $\sigma(\gamma=0)$ (weight of which is 0, not shown in Fig. 5) from $\sigma(\gamma=\pi/2)$ is about 15% within the energy range 1–10 keV/amu, but $\sigma(\gamma=0)$ decreases much more rapidly below 1 keV/amu, already by two orders of magnitude at 50 eV/amu. Therefore we consider the 90° cross sections (for oriented collisions) as a reasonable approximation and an upper bound for the randomly oriented H_2 target. Apply-

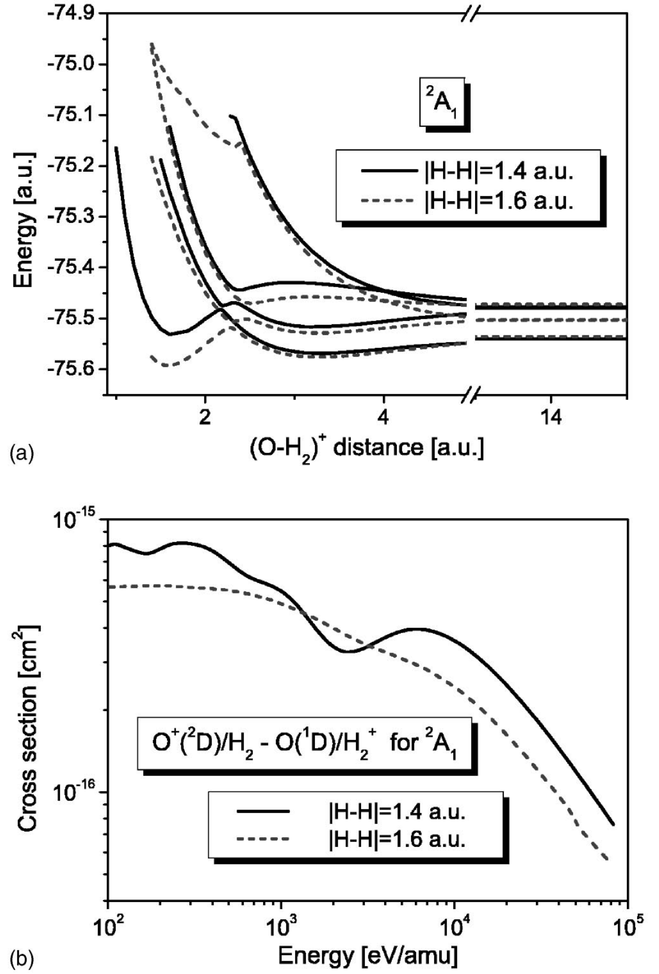

FIG. 7. $(H_2O)^+$ doublet states for $\gamma=\pi/2$: (a) $^2A_1$ potential energy curves. Solid lines: equilibrium H_2 distance. Dashed lines: $|HH|=1.6$ a.u. (b) $O^+(^2D)\rightarrow O(^1D)$ $^2A_1$ partial cross section. Solid lines: equilibrium H_2 distance. Dashed lines: $|HH|=1.6$ a.u.

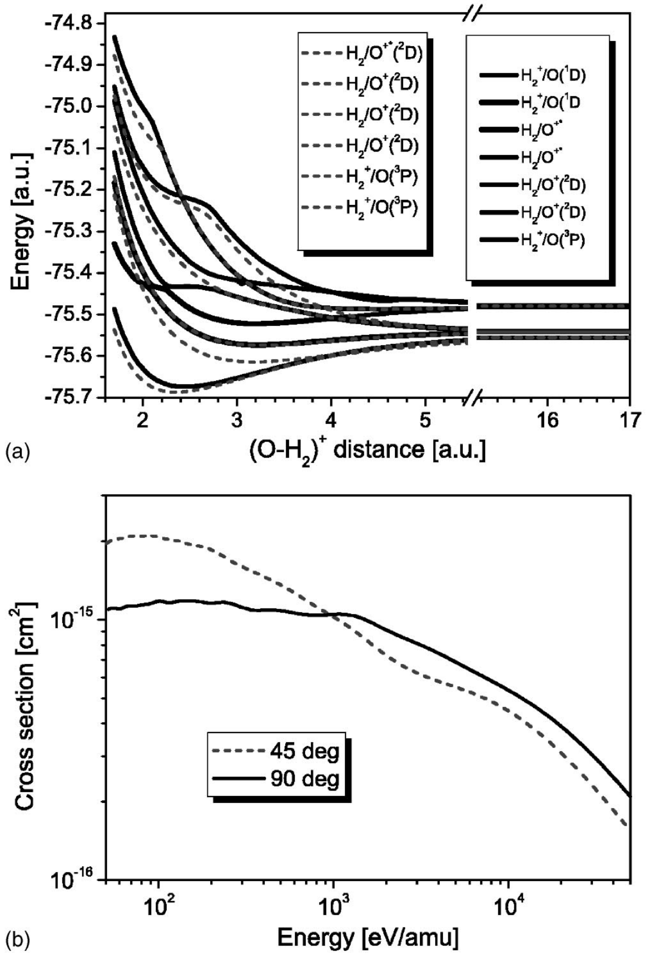

FIG. 8. (a) $(H_2O)^+$ states in C_s symmetry for $\gamma=\pi/4$ doublets. Solid lines: A' states. Dashed lines: A'' states. Labels are ordered with the energy of adiabatic potentials. (b) $O^+(^2D)$ capture cross-section amplitudes for different collision angles. Solid lines: $\gamma=\pi/2$. Dashed lines: $\gamma=\pi/4$.

ing a three-point trapezoidal rule to angle averaging suffices to estimate the order of the total electron capture from H_2 by the $O^+(^4S)$ ion in the energy region considered.

B. Electron capture by $O^{+*}(^2D)$

The metastable O^{+*} states, as compared to the $O^+(^4S)$ ground state, show an interesting γ dependence of the calculated state-resolved cross sections. Figure 6(a) gives the electron-capture cross sections to $O(^1D)$, $O(^1S)$, and $O(^3P)$ for $\gamma=\pi/2$ in various molecular-state symmetries. Cross sections for $\gamma=0$ are shown in Fig. 6(c). The total cross section $\sigma(\gamma=0)$ at low energy decreases faster than $\sigma(\gamma=\pi/2)$ due to weaker coupling terms. Also the cross section peaks tend to be more pronounced for $\gamma=0$ in the keV/amu collision energy region. No significant local minimum for the electron capture to any final state of the oxygen atom appears either for $\gamma=0$ and $\gamma=\pi/2$. The general cross-section decrease at very high energies is a physical feature which naturally appears in the basis expansion over electronic states of the molecular ion. Rapid cross-section decrease in this region is also typically obtained with the classical trajectory Monte Carlo method.

C. Electron capture by $O^{+*}(^2P)$

Electron-capture cross sections to $O(^1D)$, $O(^1S)$, and $O(^3P)$ states are shown in Fig. 6(b) for $\gamma=\pi/2$, while the case of $\gamma=0$ is plotted in Fig. 6(d). There is a substantial difference between these two cases: for $\gamma=0$, a deep cross-section minimum appears for electron capture to $O(^1D)$ for $^2\Sigma^+$ symmetry; also the cross section for electron capture to $O(^1S)$ rapidly increases with the collision energy, while the cross section for electron capture to $O(^1D)$ decreases. The cross-section dip does not appear for $\gamma=\pi/2$ for any O state and any molecular symmetry. The $^2\Sigma^+$ molecular potential energy curves corresponding to $O^{+*}(^2P)$ and $O(^1D)$ states are quasidegenerate (cf. Fig. 1, $\gamma=0$) with the Demkov type of coupling [35] near $R=5$ a.u. Then the electron capture to $O(^1D)$ occurs efficiently at low energy, while the capture cross section to $O(^1S)$ is small due to the energy gap. As the collision energy increases, this gap becomes less significant,

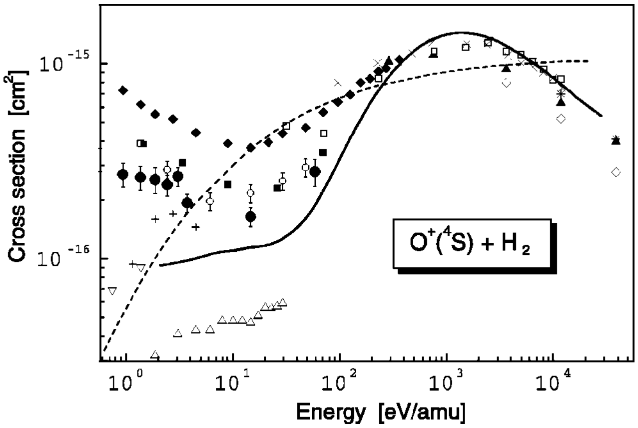

FIG. 9. $O^+(^4S)$ total charge-transfer cross-section experiments: solid circle: Kusakabe *et al.* (2001) [8]. Open circle: Kusakabe *et al.* (1990) [6]. Solid square: Sieglaff *et al.* (1999) [5]. +: Irvine and Latimer (1991) [3]. Open down triangle: Xu *et al.* (1990) [1]. Open square: Hoffman *et al.* (1982) [9]. Solid diamond: Nutt *et al.* (1979) [11]. Solid triangle: Phaneuf *et al.* (1978) [12]. ×: Lockwood *et al.* (1978) [13]. Open triangle: Moran and Wilcox (1978) [4]. Dashed line: Olson formula [19]. Solid line: present ESCC calculation.

and the probability for electron-capture transitions over a broad range of R increases.

D. H_2 target excited states

Molecular states corresponding to the charge-transfer states $O(^3S,^5S)$-H_2^+ are close in energy to the molecular state of $O^+(^4S)$-$H_2(^3\Pi)$ (cf. Ref. [22]), which facilitates the target excitation. Also electron capture from the excited H_2 molecule can be studied in this molecular-state manifold. For the sake of completeness, the calculated cross sections are shown in Fig. 6(e) (solid lines, state-resolved capture on H_2^*, dotted line, target excitation). The cross section for H_2 excitation to the $^3\Pi$ state by $O^+(^4S)$ impact is mostly about one order of magnitude lower than the major electron-capture cross sections but cannot be neglected in the high-energy region.

E. $O^{+*}(^2D) \leftrightarrow O^{+*}(^2P)$ transitions

Further processes competing with the electron transfer in O^+-H_2 collisions are projectile excitation and deexcitation. Transitions between molecular states corresponding to $O^{+*}(^2D)$ and $O^{+*}(^2P)$ occur through the sequence of two avoided crossings with the molecular state corresponding to an $O(^1D)$ molecular state, at about $R=2.4$ a.u. and $R=3.2$ a.u., with the location depending on the molecular-state symmetry. This can be clearly seen in Figs. 1 and 2 for $^2B_2$ ($\gamma=\pi/2$). Transitions through other channels contribute especially at higher energies. State-resolved projectile excitation cross sections are shown in Fig. 6(f) for $\gamma=\pi/2$ (solid lines) and $\gamma=0$ (dotted line). Transitions to the higher-lying $O^{+*}(^2P)$ state enhance the electron capture by $O^{+*}(^1D)$, as the processes discussed separately above are intertwined in this energy region.

F. Effects of target vibrations

In order to asses the effect of target molecule vibrations in the semiclassical energy region above 50 eV/amu, we have computed the potential energy surfaces for $r=1.6$ a.u. The results in Fig. 7(a) show that the potential energy curves depend rather smoothly on the H-H parametric bond length r. A uniform vertical shift of all states resulting from different r does not change the SC-ESCC probabilities, even if it is also R dependent, since this effect can be absorbed in the amplitude phases. Although the sharp coupling terms are much more sensitive to changing r, in the high-energy regime the transition amplitudes correspond to generalized Fourier integrals of the coupling terms over the entire coordinate space, which considerably diminishes the r dependence. In this case, the cross sections do not vary with r considerably, and averaging over the initial vibrational wave function yields only a multiplicative factor which is close to 1. This is well demonstrated by the partial cross section in Fig. 7(b) for the potential curves in Fig. 7(a).

Let us note at this point that vibronic couplings due to the r motion were not included in the above reasoning, which may possibly result in substantial cross-section differences below 50 eV/amu.

G. Dependence on collision angles

The multidimensional electron-capture collision problem is approximated by a set of coupled multichannel equations for each fixed angle γ. Within this framework we investigate

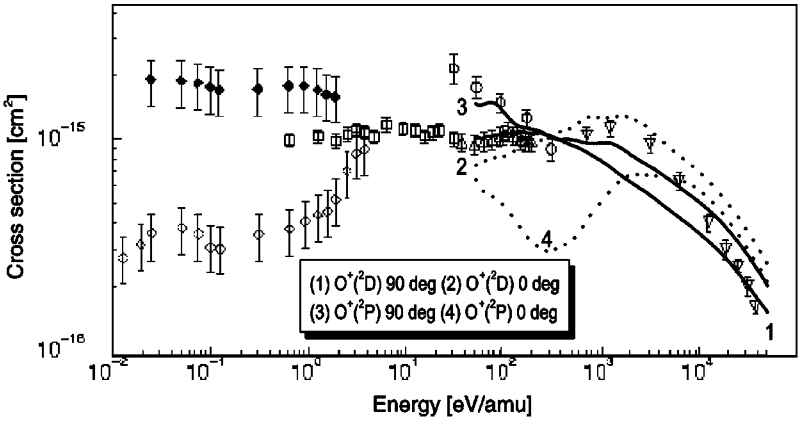

FIG. 10. $O^{+*}(^2D,^2P)$ total charge-transfer cross sections: Circle: Sieglaff *et al.* (1999) [5]. Square: Xu *et al.* (1990) [1]. Diamond: Li *et al.* [10] (open: ^2D, solid ^2P). Down triangle: Phaneuf *et al.* (1978) [12]. Triangle Moran and Wilcox (1978) [4]. SC-ESCC calculation: $O^{+*}(^2D)$ 90° (1), $O^{+*}(^2D)$ 0° (2), $O^{+*}(^2P)$ 90° (3), $O^{+*}(^2P)$ 0° (4). Solid lines: $\gamma=\pi/2$. Dotted lines: $\gamma=0$.

the cross-section dependence on the angle γ in the eikonal approximation. In addition to $\gamma=0$ (zero weight in the integral cross section) and $\gamma=\pi/2$ (maximum weight in the integral cross section), we have included the case $\gamma=\pi/4$ (H_2O^+ in C_s symmetry). The A' and A'' doublet states are plotted in Fig. 8(a). It follows from the comparison between the two cases $\gamma=\pi/2$ and $\gamma=\pi/4$ in Fig. 8(b) that the capture cross section does not depend on γ in a simple manner. With increasing energy the γ dependence generally weakens. In the energy region considered here, the cross-section differences for various γ do not affect the order of the averaged cross-section magnitude. However, large differences may arise in the lower-energy region, which can be of particular interest in the oriented ion-molecule collisions and provide more insight into the charge-transfer collision dynamics.

H. Comparison with experiments

Most of the experimental data available for O^+-H_2 collisions include, to our knowledge, differential and total charge-transfer cross sections, unresolved with respect to the final electron-capture state and target-projectile collision orientation. Yet at least the 90° collisions may be measured in principle, and new data are expected to appear in the near future. Measurements of state-resolved cross sections in various orientations should reveal new details of collision dynamics, as there is a stronger dependence on the collision energy and angle.

First, we summarize the total charge-transfer cross-section results for $O^+(^4S)$ in collisions with H_2. In Fig. 9, various experimental data for this process measured over the years are shown. The low-energy cross-section magnitude and the existence of a cross section dip at about 100 eV/amu have been in question. Previously, only the semiempirical Olson formula [19] (dashed line) was used as an estimate. Our SC-ESCC calculation is shown as the solid line. In the low-energy region, we find good agreement with the measurement of Nutt *et al.* [11], the cross-section dip measured in some experiments does not appear, and for energies above 1 keV/amu there is a general agreement between the experiment and theory. We have discussed the $O^+(^4S)$ case in a recent paper [22]. Most of the experimental difficulties are due to the uncertain production rate of O^+ metastable impurities in the ion beam, which was studied by Kusakabe *et al.* [6,8] and in previous work of Kimura *et al.* [36].

The cross sections for electron capture by the metastable O^{+*} ions are shown in Fig. 10. There is less discrepancy in the experimental data among various groups. The experimental data above 10 eV/amu were obtained in measurements on an unknown mixture of the $O^{+*}(^2D)$ and $O^{+*}(^2P)$ metastable ions. In this energy range, the experimental data should be regarded as a weighted sum of $O^{+*}(^2D)$ and $O^{+*}(^2P)$ cross-section contributions, fractions of which are unknown. Therefore theoretical cross section curves in Fig. 10 are shown separately for $O^{+*}(^2D)$ and $O^{+*}(^2P)$. Solid lines indicate the SC-ESCC cross sections calculated for $\gamma=\pi/2$, dashed lines correspond to $\gamma=0$, and the $O^{+*}(^2D)$ and $O^{+*}(^2P)$ states are distinguished. Interestingly, there is a cross section dip for the $O^{+*}(^2P)$ capture magnitude at $\gamma=0$, which is due especially to $^2\Sigma^+$ molecular states. The $O^{+*}(^2P)$ incoming channel is quasidegenerate with the $O(1D)$ capture state [cf. Fig. 1(b)], and the capture cross section to this state decreases with energy. Since the other charge-transfer state $O(^1S)$ is endothermic, the capture cross section to $O(^1S)$ for $^2\Sigma^+$ increases with energy. The combination of these two effects results in the dip of curve 4 in Fig. 10.

One order of magnitude difference in the $O^{+*}(^2D)$ and $O^{+*}(^2P)$ capture cross sections, measured by Li *et al.* [10] in the very-low-energy region about 10^{-2} eV/amu, is beyond the validity of the present treatment, as the assumptions of sudden approximation break down and also the details of the 3D potential energy surface become more important.

IV. CONCLUSION

The principal results of this paper are the state-resolved cross sections for electron capture and target-projectile electronic excitation in collisions of $O^+(^4S,{}^2D,{}^2P)$ ions with the H_2 molecule, obtained by the electronic-state close-coupling method. We have found an interesting γ dependence in the cross section for electron capture by $O^{+*}(^2P)$—namely, the existence of a pronounced dip at $\gamma=0$. The three angles considered are $\gamma=0$, $\gamma=\pi/4$, and $\gamma=\pi/2$. It is shown that the electron capture by $O^+(^4S)$ dominantly occurs in $O(^3P)$ and that no cross-section dip could be found in the $O(^3P)$, $O(^3S)$, and $O(^5S)$ charge-transfer states. In the keV/amu energy region, electronic excitations of target and projectile have a magnitude comparable to the electron capture. Total capture cross sections for $O^{+*}(^2D)$and $O^{+*}(^2P)$ are in agreement with the experimental data available for the unknown mixture of these two metastable ions. The present cross sections, both resolved and total, are considered to be useful for various applications. A systematic theoretical study of H_2O^{q+} depending on the charge q and cross-section calculations extended to the very-low-energy region are desirable for a better understanding of interstellar matter processes.

ACKNOWLEDGMENTS

We would like to thank Dr. Toshio Kusakabe for providing his manuscript prior to publication and Dr. Phillip Stancil for useful discussions. The calculation was carried in part on the Special Application Server in RIKEN. One of us (L.P.) acknowledges partial support by a JSPS Grant-in-Aid. This work was supported in part by the Ministry of Education, Science, Sport, Culture and Technology, JSPS, including the Japan-Germany collaborative program, and the National Institute for Fusion Science (L.P. and M.K.). One of us (R.J.B.) acknowledges partial support by Grant No. BU 450/7-3 of the Deutsche Forschungsgemeinschaft and the Fonds der Chemischen Industrie.

[1] Y. Xu, E. W. Thomas, and T. F. Moran, J. Phys. B **23**, 1235 (1990).
[2] G. D. Flesch and C. Y. Ng, J. Chem. Phys. **94**, 2372 (1991).
[3] A. D. Irvine and C. J. Latimer, J. Phys. B **24**, L145 (1991).
[4] T. X. Moran and J. B. Wilcox, J. Chem. Phys. **69**, 1397 (1978).
[5] D. R. Sieglaff, B. G. Lindsay, K. A. Smith, and R. F. Stebbings, Phys. Rev. A **59**, 3538 (1999).
[6] T. Kusakabe, Y. Mizumoto, K. Katsurayama, and H. Tawara, J. Phys. Soc. Jpn. **59**, 1987 (1990).
[7] T. Kusakabe *et al.*, Phys. Rev. A **60**, 344 (1999).
[8] T. Kusakabe *et al.*, J. Phys. B **34**, 4809 (2001).
[9] J. M. Hoffman, G. H. Miller, and G. L. Lockwood, Phys. Rev. A **25**, 1930 (1982).
[10] X. Li, Y.-L. Huang, G. D. Flesch, and C. Y. Ng, J. Chem. Phys. **106**, 564 (1997).
[11] W. L. Nutt, R. W. McCullough, and H. B. Gilbody, J. Phys. B **12**, L157 (1979).
[12] R. A. Phaneuf, F. W. Meyer, and R. H. McKnight, Phys. Rev. A **17**, 534 (1978).
[13] G. J. Lockwood, G. H. Miller, and J. M. Hoffman, Phys. Rev. A **18**, 935 (1978).
[14] M. Kimura and N. F. Lane, Adv. At., Mol., Opt. Phys. **26**, 79 (1989); S. A. Fuselier *et al.*, Astrophys. J. **379**, 734 (1991).
[15] A. Dalgarno, in *Molecular Processes in Space*, edited by T. Watanabe, I. Shimamura, M. Shimizu, and Y. Itikawa (Plenom, New York, 1990), p. 1.
[16] C. M. Lisse *et al.*, Science **274**, 205 (1996).
[17] R. K. Janev, in *Atomic and Molecular Processes in Fusion Edge Plasmas*, edited by R. K. Janev (Plenum, New York, 1995), p. 1.
[18] L. S. Sunderlin and P. B. Armentrout, Chem. Phys. Lett. **167**, 188 (1990).
[19] R. E. Olson, Phys. Rev. A **6**, 1822 (1972).
[20] T. E. Cravens, Science **296**, 1042 (2002).
[21] E. Speth, Rep. Prog. Phys. **52**, 57 (1989).
[22] L. Pichl, Y. Li, H.-P. Liebermann, R. J. Buenker, and M. Kimura, J. Chem. Phys. **118**, 4872 (2003).
[23] R. J. Buenker and S. D. Peyerimhoff, Theor. Chim. Acta **35**, 33 (1974); **39**, 217 (1975); R. J. Buenker, Int. J. Quantum Chem. **29**, 435 (1986).
[24] R. J. Buenker, in *Proceedings of the Workshop on Quantum Chemistry and Molecular Physics*, Wollongong, Australia, edited by P. G. Burton (Wollongong University Press, Wollongong, Australia, 1980); in *Studies in Physical and Theoretical Chemistry*, edited by R. Carbo (Elsvier, Amsterdam, 1981), Vol. 21, p. 17; R. J. Buenker and R. A. Phillips, J. Mol. Struct.: THEOCHEM **123**, 291 (1985).
[25] S. Krebs and R. J. Buenker, J. Chem. Phys. **103**, 5613 (1995).
[26] G. Hirsch, P. J. Bruna, R. J. Buenker, and S. D. Peyerimhoff, Chem. Phys. **45**, 335 (1980).
[27] T. H. Dunning, Jr., J. Chem. Phys. **90**, 1007 (1989).
[28] T. H. Dunning, Jr. and P. J. Hay, in *Methods of Electronic Structure Theory*, edited by H. F. Schaefer III (Plenum, New York, 1977), p. 1
[29] M. Kimura, Y. Li, G. Hirsch, and R. J. Buenker, Phys. Rev. A **52**, 1196 (1995); **54**, 5019 (1996).
[30] J. B. Delos, Rev. Mod. Phys. **53**, 287 (1981).
[31] V. Sidis, Adv. At., Mol., Opt. Phys. **26**, 161 (1990); M. Kimura, J. Gu, G. Hirsh, and R. J. Buenker, Phys. Rev. A **61**, 032708 (2000); P. C. Stancil, B. Zygelman, and K. Kirby, in *Photonic, Electronic, and Atomic Collisions*, edited by F. Aumayr and H. P. Winter (World Scientific, Singapore, 1998), p. 537.
[32] D. Secrest, J. Chem. Phys. **62**, 710 (1974).
[33] L. F. Errea *et al.*, Int. J. Mol. Sci. **3**, 142 (2002); L. F. Errea *et al.*, J. Phys. B **30**, 3855 (1997).
[34] D. E. Manolopoulos, M. J. Jamieson, and A. D. Pradhan, J. Comput. Phys. **105**, 169 (1993).
[35] Yu. N. Demkov, Sov. Phys. JETP **18**, 138 (1964).
[36] M. Kimura, J. P. Gu, Y. Li, G. Hirsh, and R. J. Buenker, Phys. Rev. A **49**, 3131 (1994).